The Astrophysical Journal Letters, 727:L30 (6pp), 2011 February 1 doi:10.1088/2041-8205/727/2/L30

MESOGRANULATION AND THE SOLAR SURFACE MAGNETIC FIELD DISTRIBUTION

L. Yelles Chaouche[1,2], F. Moreno-Insertis[1,2], V. Martínez Pillet[1], T. Wiegelmann[3], J. A. Bonet[1,2], M. Knölker[4,5], L. R. Bellot Rubio[6], J. C. del Toro Iniesta[6], P. Barthol[3], A. Gandorfer[3], W. Schmidt[5], and S. K. Solanki[3,7]
[1] Instituto de Astrofisica de Canarias, Via Lactea, s/n, 38205 La Laguna (Tenerife), Spain
[2] Department of Astrophysics, Universidad de La Laguna, 38200 La Laguna (Tenerife), Spain
[3] Max-Planck-Institut für Sonnensystemforschung, Max-Planck-Strasse 2, 37191 Katlenburg-Lindau, Germany
[4] High Altitude Observatory (NCAR), Boulder, CO 80307, USA
[5] Kiepenheuer-Institut für Sonnenphysik, 79104 Freiburg, Germany
[6] Instituto de Astrofisica de Andalucia (CSIC), Glorieta de la Astronomia, s/n 18008 Granada, Spain
[7] School of Space Research, Kyung Hee University, Yongin, Gyeonggi 446-701, Republic of Korea
Received 2010 November 16; accepted 2010 December 15; published 2011 January 4

ABSTRACT

The relation of the solar surface magnetic field with mesogranular cells is studied using high spatial (≈100 km) and temporal (≈30 s) resolution data obtained with the IMaX instrument on board SUNRISE. First, mesogranular cells are identified using Lagrange tracers (corks) based on horizontal velocity fields obtained through local correlation tracking. After ≈20 minutes of integration, the tracers delineate a sharp mesogranular network with lanes of width below about 280 km. The preferential location of magnetic elements in mesogranular cells is tested quantitatively. Roughly 85% of pixels with magnetic field higher than 100 G are located in the near neighborhood of mesogranular lanes. Magnetic flux is therefore concentrated in mesogranular lanes rather than intergranular ones. Second, magnetic field extrapolations are performed to obtain field lines anchored in the observed flux elements. This analysis, therefore, is independent of the horizontal flows determined in the first part. A probability density function (PDF) is calculated for the distribution of distances between the footpoints of individual magnetic field lines. The PDF has an exponential shape at scales between 1 and 10 Mm, with a constant characteristic decay distance, indicating the absence of preferred convection scales in the mesogranular range. Our results support the view that mesogranulation is not an intrinsic convective scale (in the sense that it is not a primary energy-injection scale of solar convection), but also give quantitative confirmation that, nevertheless, the magnetic elements are preferentially found along mesogranular lanes.

Key words: Sun: granulation – Sun: magnetic topology – Sun: photosphere – Sun: surface magnetism

Online-only material: color figures

1. INTRODUCTION

Mesogranulation was historically introduced as a prominent scale imprinted on the horizontal photospheric flows calculated through local correlation tracking (LCT) of intensity images (November et al. 1981; Simon et al. 1988; Brandt et al. 1988, 1991; Muller et al. 1992; Roudier et al. 1998, 1999; Shine et al. 2000; Leitzinger et al. 2005): both the pattern of positive and negative divergence of that flow and the time evolution of Lagrange tracers moving in it revealed cells with sizes between, say, 5 and 10 arcsec. Much debate ensued concerning whether the mesogranular flow patterns correspond to actual convection cells in that range of sizes rather than, e.g., to simple granule associations which persist in time (see, e.g., Cattaneo et al. 2001; Roudier et al. 2003; Roudier & Muller 2004; Nordlund et al. 2009; Matloch et al. 2009, 2010). Independent hints for the existence of a convective flow operating on those scales are therefore of importance. The study of the surface distribution of magnetic elements can provide such hints; as a minimum, it can constitute an alternative avenue, independent of the inaccuracies of LCT methods, to determine the properties of the mesogranular patterns. Such an approach has been employed by Domínguez Cerdeña et al. (2003), Domínguez Cerdeña (2003), and Sánchez Almeida (2003) using ground-based data and by Roudier et al. (2009) and Ishikawa & Tsuneta (2010) using satellite observations. In those papers, visual evidence was obtained that there is an association between magnetic flux structures (flux elements, transient horizontal fields) and the mesogranular pattern obtained through the study of horizontal flows. Yet, detailed quantitative studies and statistics that could put such an association on a firmer basis are still missing.

The aim of this Letter is to obtain quantitative information of the relation between photospheric magnetic flux distributions and mesogranular scales by using the observations of unprecedented quality provided by the Imaging Magnetograph eXperiment (IMaX; Martinez Pillet et al. 2010) on board the SUNRISE balloon-borne observatory (Barthol et al. 2010; Solanki et al. 2010). IMaX provides time series of virtually seeing-free high spatial resolution (0.15 arcsec) images and magnetograms that constitute an ideal data set for the study of photospheric magnetism. Using the SUNRISE/IMaX data, we combine information from (1) the velocity field gained through LCT of intensity images; (2) the spatial patterns provided by the magnetograms; and (3) the field line structure obtained through extrapolation of the magnetogram data, to gain quantitative information concerning patterns at intermediate scales between granulation and supergranulation.

2. DATA

For this study, we use sequences of images recorded with IMaX near the solar disk center on 2009 June 9. Images were taken at five wavelengths along the profile of the magnetic-sensitive Fe I 5250.2 Å line located at ±80 mÅ, ±40 mÅ from line center, and continuum at +227 mÅ. The estimated circular polarization noise is 5×10^{-4} in units of the continuum

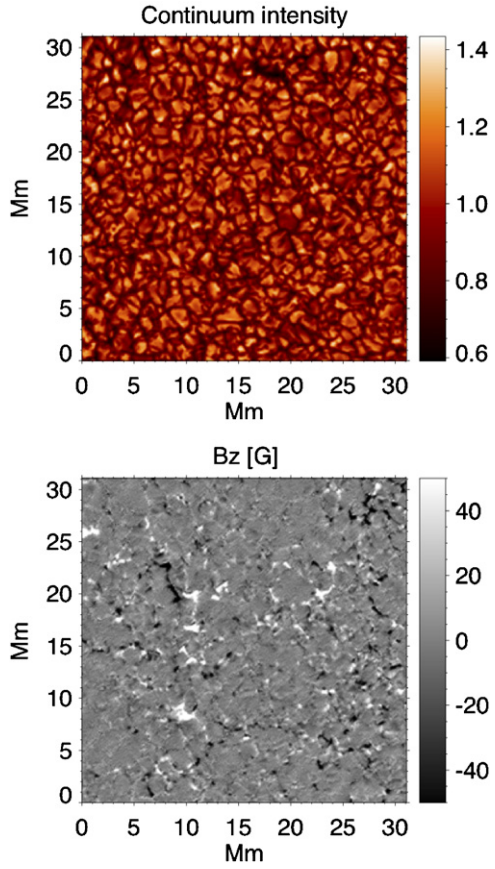

Figure 1. Top: normalized continuum intensity near the spectral line Fe I 5250.2 Å. Bottom: vertical component of the magnetic field vector (B_z) retrieved from inversions and clipped at ±50 G. The maps are taken from the first observed time series.

(A color version of this figure is available in the online journal.)

wavelength for non-reconstructed data and three times larger for the reconstructed one. IMaX has a spectral resolution of 85 mÅ and a spatial resolution of ∼100 km (Martinez Pillet et al. 2010). The reduction procedure produces time series of images with a cadence of 33.25 s, spatial sampling of 39.9 km, and a field of view (FOV) of 32 × 32 Mm^2. We use two time series, the first one comprising 42 snapshots (23 minutes) and the second one 58 snapshots (32 minutes). Magnetograms are derived from inversions of the observed Stokes parameters using the SIR code (Ruiz Cobo & del Toro Iniesta 1992). We call these magnetograms the reconstructed data. In this Letter, we mainly use the reconstructed data except in the last section (Section 5) where, in addition, we use so-called calibrated data, i.e., magnetograms obtained using a proportionality law between Stokes-V (from non-reconstructed data) and B_z (for details of this method, see Martinez Pillet et al. 2010). The intensity maps are taken from the reconstructed data.

Figure 1 displays a map of normalized continuum intensity (top) and the corresponding longitudinal magnetogram (bottom), the latter showing many internetwork flux concentrations alongside stronger flux elements probably belonging to the network.

3. MESOGRANULATION AND HORIZONTAL FLOWS

Following the traditional method, mesogranular patterns are outlined by using Lagrange tracers (popularly known as corks) arranged at time $t = 0$ uniformly in a two-dimensional grid that

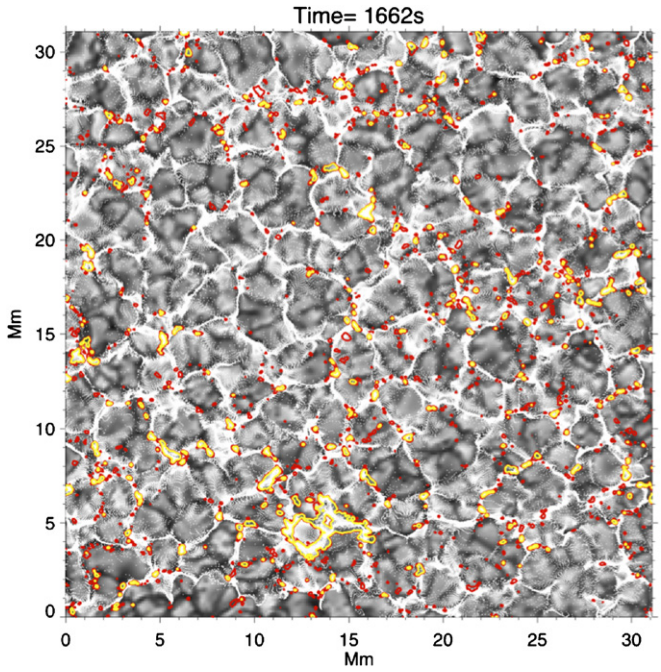

Figure 2. Cork distribution (white dots) outlining mesogranular cells at $t =$ 28 minutes. The background image is continuum intensity. Color lines: $|B_z|$ contours for 30 G (red) and 50 G (yellow).

(A color version of this figure is available in the online journal.)

coincides with the observational pixel matrix. Then, the corks are advected following the instantaneous horizontal velocity field along the whole duration of the time series (here we use the second time series: 32 minutes). The horizontal velocity field is determined using the LCT algorithm by Welsh et al. (2004) applied to consecutive continuum intensity images. The correlation is performed in local windows weighted by a Gaussian function with FWHM = 320 km. Often, in the literature, the velocity field determined through LCT and used to advect corks is a time average of the noisy determinations of the instantaneous velocity fields for consecutive snapshots (for a discussion about the effect of time averaging see, e.g., Rieutord et al. 2000, 2001). The high signal-to-noise ratio, the high spatial and temporal resolution, and the absence of atmospheric distortion in the IMaX data make it possible to evaluate clean velocity fields and consequently to compute cork advection without time averaging.

In Figure 2 we show (white dots) the distribution of corks at $t = 28$ minutes, i.e., toward the end of the series, on the background of the continuum intensity image at that time. The corks clearly delineate cells of mesogranular size containing several granules. In fact, the vast majority of corks are located in the lanes between those cells (which we will call here mesogranular lanes or mesolanes for short). A clear mesogranular pattern with the majority of the corks concentrated in mesolanes is already visible after only some 20 minutes from $t = 0$. This is less than the time (2–4 hr) reported by Roudier et al. (2009) using the *Hinode*/SOT NarrowBand Filter Imager.

In order to obtain quantitative measures for the mesogranular network we define a cork density function, $\rho_{\rm cork}$, by counting the number of corks in each pixel in the image. To provide an upper bound for the width of the mesolanes, we scan the image vertically using whole horizontal lines and calculate the width ($1/e$ of the maximum) of the peaks of the $\rho_{\rm cork}$ function in each line. We then derive an average peak width for the whole scan.

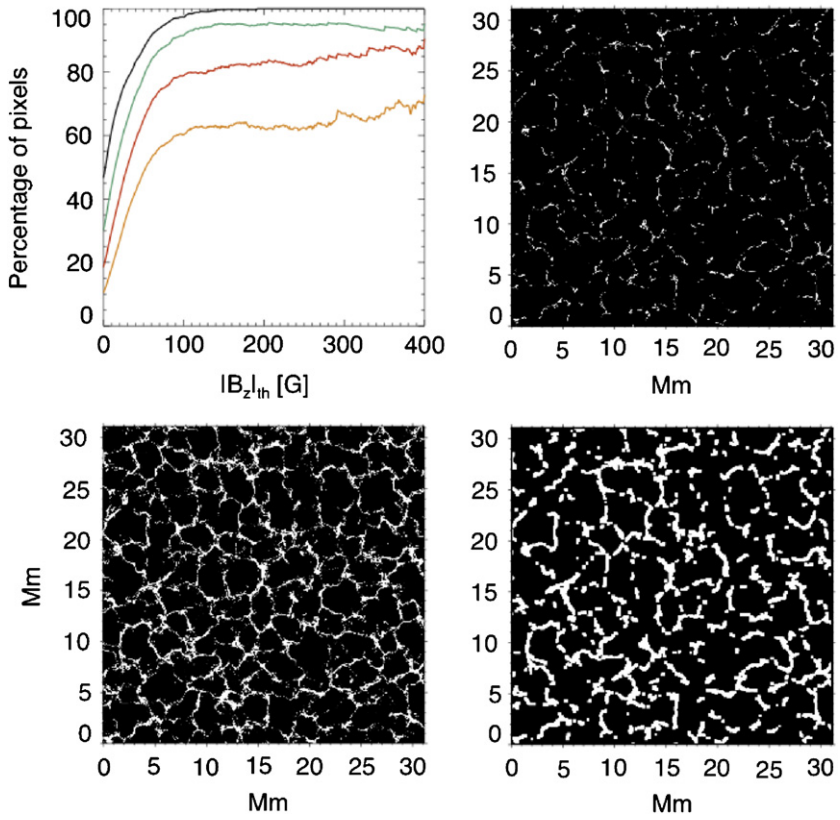

Figure 3. Top left: percentage of pixels with $|B_z|_{\rm th}$ above the value given in abscissas located within 3 pixels (∼120 km) from mesolanes. Mesolanes are defined through $\rho_c > 2, 4, 8, 16$ corks pixel^{-1} for the black, green, red, and orange curves, respectively. Top right and bottom left panels: distribution of pixels with $\rho_c > 8$ (top right) and $\rho_c > 2$ (bottom left) corks pixel^{-1}, respectively. Bottom right panel: 3 pixel neighborhood of the points shown in the top right panel. The calculations are done for similar time as Figure 2 ($t = 28$ minutes).

(A color version of this figure is available in the online journal.)

If we use all peaks above $\rho_{\rm cork} = 10$, then the resulting upper bound for the lane width is 285 km. The largest concentrations of corks are located in narrow mesolanes: using all peaks above $\rho_{\rm cork} = 30$, for instance, yields a width of 180 km (4.5 pixels). Given the random orientation of the mesolanes, their actual width is certainly below those numbers. Using a horizontal scan instead of a vertical one yields basically the same numbers (the maximum deviation is 7%).

4. CORRELATION BETWEEN MESOGRANULAR LANES AND FIELD CONCENTRATIONS

A first test of the relation between mesogranules and the surface magnetic field can be obtained by studying the spatial association between mesogranular cells and magnetic flux concentrations. Through visual inspection, various researchers have obtained indications that the magnetic field concentrations with higher flux density are distributed at the boundaries of cells of mesogranular size (5–10 arcsec; see Domínguez Cerdeña et al. 2003; Sánchez Almeida 2003); in fact, Domínguez Cerdeña (2003) shows the preference of elements with flux density above 60 G to be located in regions of high negative divergence of the horizontal velocity. Further visual evidence is provided by Roudier et al. (2009) who plot Stokes-V images obtained with *Hinode*/NFI on top of cork distributions showing a relationship between magnetic field concentrations and cork lanes (see also de Wijn et al. 2005; Solanki et al. 2010).

The conclusions at that level can be reinforced through our high-resolution maps by drawing contours of $|B_z|$ down to small values, like 30 G. The red and yellow contours in Figure 2 correspond to flux density values of 30 and 50 G, respectively. The figure exhibits flux concentrations mostly located at mesolanes. One can note that flux concentrations with higher flux density (yellow contours: 50 G) correlate better with mesolanes.

Going one step further, we can obtain quantitative estimates to test the visual impression gained by combining cork images and magnetograms. We use as a proxy for the mesolanes the locations with cork density above a threshold, $\rho_c > \rho_{c0}$, and use the values $\rho_{c0} = 2, 4, 8, 16$ corks pixel^{-1}. All of those values yield clear mesogranular lanes, as apparent, e.g., in the top right and bottom left panels of Figure 3, drawn for $\rho_{c0} = 8$ and 2, respectively. Increasing ρ_{c0} decreases the level of connectivity of the lanes. We then focus on the mesolanes defined by $\rho_c > \rho_{c0} = 8$ and study which fraction of the magnetic elements are really in (or near) them. To obtain a quantitative estimate, for each fixed threshold intensity $|B_z|_{\rm th}$ in the range (0, 400) G, we consider the set of pixels with $B > |B_z|_{\rm th}$ and calculate which fraction of the set is located in 3 pixel neighborhoods of the mesolanes. The result is shown in the top left panel of Figure 3 (red curve). The curve reaches an approximate horizontal asymptote at the 85% level for $|B_z|_{\rm th}$ above 100 G. The other curves in the figure contain the same results but using $\rho_{c0} = 2$ (black curve), 4 (green), and 16 (orange). We see approximate horizontal asymptotes in all cases, and all are reached for $|B_z|_{\rm th}$ between 80 and 100 G. We conclude that the vast majority of pixel elements with $B \gtrsim 100$ G is located in the near neighborhood of

locations with high cork density. For the least restrictive case ($\rho_{c0} = 2$), virtually all magnetic elements with $B \gtrsim 100$ G are located in the neighborhood of the mesolanes. For large ρ_{c0} (e.g., $\rho_{c0} = 16$ corks pixel^{-1}; orange curve), the resulting areas have less connectivity and do not delineate so clearly the mesogranular network. Correspondingly, the asymptotic percentage values for $B \gtrsim 100$ G become smaller. The width of the 3 pixel neighborhoods of the mesolanes is shown in the bottom right panel for the $\rho_{c0} = 8$ corks pixel^{-1} case. The panel shows a fully developed network of mesolanes covering only 17% of the whole surface (which, of course, coincides with the $|B_z|_{\rm th} \rightarrow 0$ limit of the red curve). As an aside note, all curves remain basically the same if we remove the prominent network element located in the lower part of Figure 2.

5. THE SEPARATION BETWEEN THE FOOTPOINTS OF EXTRAPOLATED FIELD LINES

5.1. Method

As a further test of the relation between surface fields and convection at different scales, in this section we study the statistics of footpoint separation between field lines linking the magnetic elements observed with IMaX. To that end, we calculate the magnetic field vector in the atmosphere using force-free field extrapolations from the IMaX data. We use a code with weighted optimization method (Wiegelmann 2004; see also Seehafer 1978). The force-free assumption is equivalent to assuming that the electrical current **j** and the magnetic field **B** are parallel, or, using Ampère's law:

$$\nabla \times \mathbf{B} = \frac{4\pi}{c}\mathbf{j} = \alpha\,\mathbf{B}, \qquad (1)$$

α in Equation (1) measures the level of field line twist. The field values obtained with the IMaX data correspond to the height where the Fe I 5250.2 Å line is formed. Although the photosphere is not a small-β plasma (with β being the ratio of gas to magnetic pressures), there are theoretical and observational indications (Wiegelmann et al. 2010a, 2010b; Martínez González et al. 2010) that the force-free assumption is acceptable when calculating extrapolations starting from those heights. We will be using $\alpha = 0.1/L$, with $L \times L$ being the IMaX FOV. In any case, Wiegelmann et al. (2010b), using the same IMaX data, show that values of α in the range $(-4/L, 4/L)$lead to similar values in the statistical properties they analyzed for the extrapolated field lines.

For computational reasons, we have calculated the extrapolations in a box of 389 × 389 × 389 equally spaced grid points, keeping the original horizontal dimensions, leading to a cell size of ≈80 km. Yet, test calculations with the original number of grid points (778 in each direction) yield essentially the same results.

An example of magnetic field lines is shown in Figure 4. A map of the vertical magnetic field component is shown at the bottom of the box corresponding to a region of about 10 × 10 Mm^2 centered on the point $(x, y) = (10, 20)$ Mm in Figure 1. The field line footpoints are seen to cluster on field concentrations in the domain. In agreement with the conclusions of Wiegelmann et al. (2010b), this figure shows a rough proportionality between the footpoint distance and the height reached by the field lines.

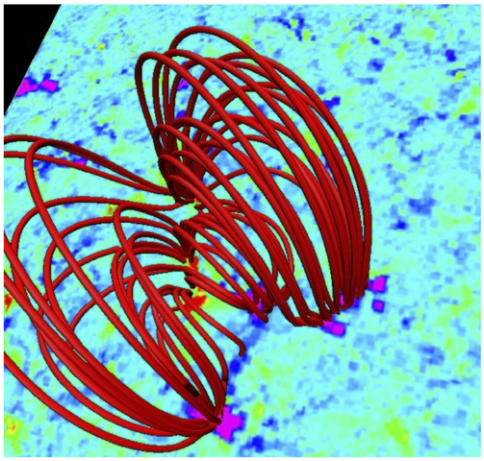

Figure 4. Magnetic field lines showing the connectivity between flux concentrations. Background image: map of B_z (purple and blue: $B_z > 0$; green and red: $B_z < 0$). The background image is a ≈10 × 10 Mm^2 patch around the point (10, 20) Mm in Figure 1.

(A color version of this figure is available in the online journal.)

5.2. Statistics of Footpoint Separation

Calling x the distance between footpoints, we calculate the probability density function (PDF) for x using as statistical ensemble for each time series the field lines in each snapshot and the whole collection of snapshots in the series. To include a field line in the study, we request a flux density above 15 G on both footpoints. The resulting PDFs are shown in Figure 5. The black and red lines correspond to the first and second time series, respectively. Additionally, we plot PDFs for distances between field line footpoints calculated by extrapolating calibrated data following Martinez Pillet et al. (2010), as explained in Section 2, which involves no inversion procedure (yellow and green curves, for the first and second time series, respectively). All the curves approximately fit an exponential distribution at scales between 1 and 10 Mm, i.e., at granular and mesogranular scales; the slope is $d\log(\mathrm{PDF})/dx \approx -0.6$ Mm^{-1}. Beyond 10 Mm, at supergranular scales, the curves show a deviation from the exponential. This *bump* most probably corresponds to the presence in that time series of strong network elements. Anyway, given the size of the IMaX FOV (≈30 Mm) and the long duration of the largest convection cells, we cannot draw statistical inferences from the PDF for scales above, say, 10 Mm. On the other hand, we have carried out a Kolmogorov–Smirnov test of the goodness of fit of the footpoint distance data in the 1–10 Mm range to a lognormal distribution, additionally to the exponential distribution; a lognormal distribution is found to fit magnetogram data well or, more generally, data resulting from the fragmentation of magnetic elements (Abramenko & Longcope 2005; see also Bogdan et al. 1988). In our case, the test, carried out for individual snapshots in the given distance range, favors the exponential distribution. Details of this analysis will be given in a publication in preparation.

We note the constancy of the slope of the PDF at scales between 1 and 10 Mm and that the characteristic decay distance is approximately 1.7 Mm. This is probably a consequence of the fact that there are no intrinsic horizontal scales in that range other than granulation, e.g., because mesogranulation is the direct result of other convection scales, rather than representing a primary scale in which energy is being injected into the convective flows.

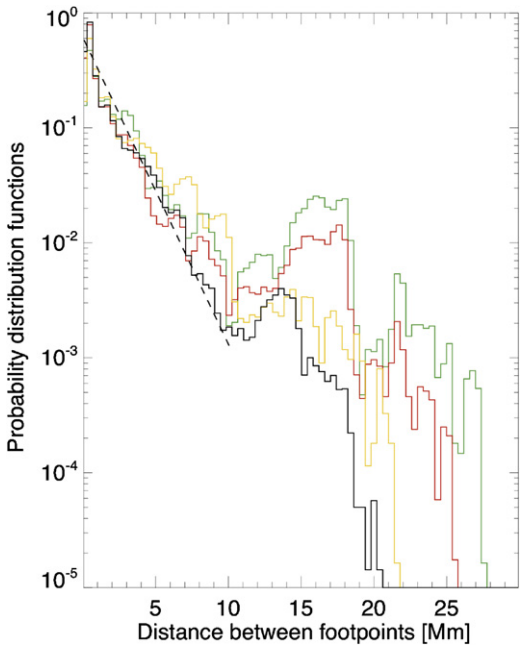

Figure 5. Probability density functions of the distance between footpoints of field lines. Black and yellow: data from the first time series (inverted data: black; data calibrated following Martinez Pillet et al. (2010): yellow). Red and green: same as black and yellow, but for series 2. The straight dashed line represents an exponential fit of the black curve for the first ≈10 Mm.

(A color version of this figure is available in the online journal.)

6. DISCUSSION AND CONCLUSIONS

An important open question in solar physics is the precise nature of the convection scales with size and duration above the granular values. While both granulation and supergranulation yield velocity field patterns that have been observed at the surface, mesogranules have been detected only through indirect proxies, like tracking of intensity patterns, which do not provide reliable evidence of underlying convection cells in that range of sizes and durations. There is an ongoing debate on whether there is a continuum of sizes for the convection cells on scales above granular, possibly with self-similar properties and with no particular scale being singled out within that range (Nordlund et al. 2009), or whether the mesogranular scales are just the result of a collective interaction between families of granules. The magnetic field can provide an alternative and more direct avenue to explore convective patterns since the magnetic flux can be measured directly using Stokes polarimetry techniques. The magnetic elements appear with a broad spectrum of flux densities (Orozco Suárez et al. 2007; Khomenko et al. 2003) and can also be detected through *G*-band or Ca II bright points (see de Wijn et al. 2005; Sánchez Almeida et al. 2010) and therefore can provide important clues concerning the nature of the flows underlying the mesogranular scales as well as about the magnetic elements themselves.

The high spatial and temporal cadences of the IMaX data allow us to try a few different, complementary studies of the relation between magnetic field and mesogranular flows. First, we have carried out Lagrange tracing of mass elements following horizontal flow fields obtained through LCT of intensity maps; we have obtained a number of improvements compared with traditional cork maps (faster development of the mesogranular lanes, no need for time averages). We have also obtained an upper bound for the width of the mesogranular lanes of some 280 km. Second, we have provided quantitative measures for the association between magnetic elements and mesogranular lanes. The large majority (85%) of the magnetic elements with flux density above ∼100 G are found in 120 km neighborhoods of mesogranular lanes with $\rho_c > 8$ and about 80% of flux elements above 30 G are located near mesogranular lanes with $\rho_c > 2$. Our results indicate a good coupling between the flow field and the magnetic elements, suggesting that the evolution of the latter is mostly kinematic. Third, we have considered the connectivity between magnetic elements and, in particular, the distance between footpoints of field lines anchored in the photosphere. The PDF of such distances shows that there is abundant connectivity on mesogranular scales; it also shows that the distribution is basically featureless in those scales, with only one characteristic value, the slope of the distribution, equal to $(1.7\,\mathrm{Mm})^{-1}$.

Our results concerning statistics of separations of field line footpoints suggest that there is no intrinsic scale of convection in the mesogranular range. This may only mean that there is no mechanism for direct injection of energy into convection on those scales, but does not rule out the existence of convection cells with those sizes, e.g., through nonlinear interactions of cells at other scales (as in a turbulent cascade) or through the interaction of thermal downflows (Rast 2003).

Financial support by the European Commission through the SOLAIRE Network (MTRN-CT-2006-035484) and by the Spanish Ministry of Research and Innovation through projects AYA2007-66502, CSD2007-00050, and AYA2007-63881 is gratefully acknowledged, as are the computer resources, technical expertise, and assistance provided by the MareNostrum (BSC/CNS, Spain) supercomputer installation. L.Y.C. and F.M.-I. are grateful to V. Abramenko for advice concerning the Kolmogorov–Smirnov test of statistical distributions. The German contribution to SUNRISE is funded by the Bundesministerium für Wirtschaft und Technologie through DLR Grant 50 OU 0401, and by the Innovationsfond of the President of the Max Planck Society (M.P.G.). The Spanish contribution has been funded by the Spanish MICINN under projects ESP2006-13030-C06 and AYA2009-14105-C06. The HAO contribution was partly funded through NASA grant number NNX08AH38G. This work has been partially supported by WCU grant no. R31-10016 funded by the Korean Ministry of Education, Science and Technology.

REFERENCES

Abramenko, V. I., & Longcope, D. W. 2005, ApJ, 619, 1160
Barthol, P., et al. 2010, Sol. Phys., 268, 57
Bogdan, T. J., Gilman, P. A., Lerche, I., & Howard, R. 1988, ApJ, 327, 451
Brandt, P. N., Ferguson, S., Shine, R. A., Tarbell, T. D., & Scharmer, G. B. 1991, A&A, 241, 219
Brandt, P. N., Scharmer, G. B., Ferguson, S., Shine, R. A., & Tarbell, T. D. 1988, Nature, 335, 238
Cattaneo, F., Lenz, D., & Weiss, N. 2001, ApJ, 563, L91
de Wijn, A. G., Rutten, R. J., Haverkamp, E. M. W. P., & Sütterlin, P. 2005, A&A, 441, 1183
Domínguez Cerdeña, I. 2003, A&A, 412, L65
Domínguez Cerdeña, I., Sánchez Almeida, J., & Kneer, F. 2003, A&A, 407, 741
Ishikawa, R., & Tsuneta, S. 2010, ApJ, 718, L171
Khomenko, E. V., Collados, M., Solanki, S. K., Lagg, A., & Trujillo Bueno, J. 2003, A&A, 408, 1115
Leitzinger, M., Brandt, P. N., Hanslmeier, A., Pötzi, W., & Hirzberger, J. 2005, A&A, 444, 245
Martínez González, M. J., Manso Sainz, R., Asensio Ramos, A., & Bellot Rubio, L. R. 2010, ApJ, 714, L94
Martinez Pillet, V., et al. 2010, Sol. Phys., 268, 57
Matloch, L., Cameron, R., Schmitt, D., & Schüssler, M. 2009, A&A, 504, 1041

Matloch, Ł., Cameron, R., Shelyag, S., Schmitt, D., & Schüssler, M. 2010, A&A, 519, A52
Muller, R., Auffret, H., Roudier, T., Vigneau, J., Simon, G. W., Frank, Z., Shine, R. A., & Title, A. M. 1992, Nature, 356, 322
Nordlund, Å., Stein, R. F., & Asplund, M. 2009, Living Rev. Solar Phys., 6, 2
November, L. J., Toomre, J., Gebbie, K. B., & Simon, G. W. 1981, ApJ, 245, L123
Orozco Suárez, D., et al. 2007, ApJ, 670, L61
Rast, M. P. 2003, ApJ, 597, 1200
Rieutord, M., Roudier, T., Ludwig, H., Nordlund, Å., & Stein, R. 2001, A&A, 377, L14
Rieutord, M., Roudier, T., Malherbe, J. M., & Rincon, F. 2000, A&A, 357, 1063
Roudier, T., Lignières, F., Rieutord, M., Brandt, P. N., & Malherbe, J. M. 2003, A&A, 409, 299
Roudier, T., Malherbe, J. M., Vigneau, J., & Pfeiffer, B. 1998, A&A, 330, 1136
Roudier, T., & Muller, R. 2004, A&A, 419, 757
Roudier, T., Rieutord, M., Brito, D., Rincon, F., Malherbe, J. M., Meunier, N., Berger, T., & Frank, Z. 2009, A&A, 495, 945
Roudier, T., Rieutord, M., Malherbe, J. M., & Vigneau, J. 1999, A&A, 349, 301
Ruiz Cobo, B., & del Toro Iniesta, J. C. 1992, ApJ, 398, 375
Sánchez Almeida, J. 2003, A&A, 411, 615
Sánchez Almeida, J., Bonet, J. A., Viticchié, B., & Del Moro, D. 2010, ApJ, 715, L26
Seehafer, N. 1978, Sol. Phys., 58, 215
Shine, R. A., Simon, G. W., & Hurlburt, N. E. 2000, Sol. Phys., 193, 313
Simon, G. W., Title, A. M., Topka, K. P., Tarbell, T. D., Shine, R. A., Ferguson, S. H., & Zirin, H. SOUP Team 1988, ApJ, 327, 964
Solanki, S. K., et al. 2010, ApJ, 723, L127
Welsh, B. T., Fisher, G. H., Abbett, W. P., & Regnier, S. 2004, ApJ, 610, 1148
Wiegelmann, T. 2004, Sol. Phys., 219, 87
Wiegelmann, T., Yelles Chaouche, L., Solanki, S. K., & Lagg, A. 2010a, A&A, 511, A4
Wiegelmann, T., et al. 2010b, ApJ, 723, L185